Applied Surface Science 717 (2026) 164732

Contents lists available at ScienceDirect

Applied Surface Science

journal homepage: www.elsevier.com/locate/apsusc

Full Length Article

A hybrid density functional theory investigation of silicon and germanium at the (100) diamond surface: routes to stable negative electron affinity for electron-emission applications

Neil L. Allan, Paul W. May *

School of Chemistry, Cantock's Close, Bristol BS8 1TS, United Kingdom

ARTICLE INFO

Keywords:
CVD diamond
Negative electron affinity
Silicon termination
Germanium termination
Thermionic emission

ABSTRACT

Termination of the diamond (100) surface with silicon and germanium is modelled using hybrid density functional theory (DFT) for coverages up to 1 monolayer (ML). Adsorption energies and electron affinities were calculated using the B3LYP exchange–correlation functional. Calculations predict that all configurations except one possess a negative electron affinity (NEA). In general, Si adsorption results in slightly higher exothermic adsorption energies, but Ge adsorption produces surfaces with larger NEA values. Additionally, we quantify the charge transfer from the adsorbates to the diamond surface using both Mulliken and Bader's "atoms-in-molecules" charge partitioning (QTAIM) analyses. We suggest that the suppressed NEA in the case of Si may be the result of the more negative atomic basin dipole moments for Si.

1. Introduction

The advent of chemical vapour deposition of diamond [1,2] has now established diamond as an exceptional engineering material useful for a wide range of technological applications [3]. The adsorption of species on a diamond surface in order to enhance its electron emission properties has been extensively explored both experimentally and theoretically [4], with applications pertaining to energy generation, photodiodes, secondary electron emission, and surface transfer doping, *etc*. [5–9]. One of the most exciting potential applications for this material is as the electron source in a thermionic energy converter (TEC) [10]. In such a device, solar radiation is focused by means of a solar-tracking parabolic mirror onto a diamond cathode, heating it to high temperatures sufficient to cause electrons to be thermionically emitted from its surface. Depending upon the species terminating its surface, diamond is one of the rare materials that can exhibit so-called negative electron affinity (NEA), which means that no energy barrier needs to be overcome for electrons residing in the conduction band to escape into vacuum. As a result, the temperatures required for thermionic electron emission from diamond (~900 °C) are substantially lower than those needed for metals such as tungsten (1500–2000 °C), making diamond thermionic devices more efficient and easier to fabricate than most other competing materials

In a TEC, the emitted electrons travel across a vacuum gap and are collected by a cooler anode. The difference in work function between the anode and cathode creates a potential difference between the electrodes. Connecting them together completes the circuit, and permits electrons to flow from the anode back to the cathode, driving an electric current through a load. Thus, heat is converted directly into electricity within a solid-state device that has no moving parts. Solar TECs, such as this, could provide an alternative, complementary technology to standard photovoltaic solar cells for renewable energy generation.

However, the key to this technology is to develop a diamond surface that has both a large NEA (and therefore a low work function) and which remains stable at the high temperatures needed for thermionic emission. Both natural and lab-grown diamond have surface carbon atoms which are terminated with hydrogen, which creates a reasonable NEA of around −1 eV. Unfortunately, H desorbs from the diamond surface at only around 500 °C, removing the NEA and making it unsuitable for thermionic applications. As such, the last few years have seen a growing number of theoretical and experimental studies to identify and characterise alternative diamond terminations that are compatible with TECs [4].

Theoretical investigations of adsorbates on diamond surfaces typically employ *ab initio* density function theory (DFT) methods to predict structural arrangements, as well as other energetic and electronic

* Corresponding author.
E-mail address: Paul.May@bristol.ac.uk (P.W. May).

https://doi.org/10.1016/j.apsusc.2025.164732
Received 13 May 2025; Received in revised form 12 September 2025; Accepted 25 September 2025
Available online 27 September 2025

properties of the diamond-adsorbate system. These investigations have used different DFT codes, such as CASTEP [11–15], AIMPRO [16] and CRYSTAL [17,18], and often exploit a range of methodologies and different exchange–correlation (XC) functionals. One of the most salient properties predicted in these DFT investigations has been the electron affinity (EA), χ, which is defined as the difference in energy between the vacuum level, E_{vac}, and that of the conduction band minimum (CBM), E_{CBM}:

$$\chi = E_{vac} - E_{CBM} \quad (1)$$

A positive electron affinity (PEA), where $E_{vac} > E_{CBM}$, means that electrons situated in the conduction band experience an energy barrier to emission from the surface of the material that is equal to the PEA, as shown in Fig. 1. In contrast, for an NEA where $E_{vac} < E_{CBM}$, electrons at the CBM experience no emission barrier. The origin of PEA or NEA at diamond surfaces is frequently ascribed to the formation of a surface dipole which originates due to differences in the electronegativity of the adsorbing species and the bulk carbon. If the electronegativity of the adsorbate is more negative than that of carbon, a surface dipole is formed with the negative charge outermost, which repels electrons back into the bulk, resulting in a PEA. Conversely, when the adsorbate is more electropositive than carbon, the surface dipole has its positive charge outermost, which is believed to assist the escape of electrons into vacuum, resulting in an NEA.

The most obvious candidates for electropositive adsorbates are metal atoms. Group I metals, do indeed, exhibit NEA characteristics when adsorbed on diamond, but the larger metals in the group, such as Cs, have low thermal stability which limits their usefulness at higher temperatures [19]. As such, work has focused upon smaller Group I metals, such as Li [12,20] as well as various first-row transition metals (TMs), including Cu, Ni, Ti, V and Zn [21–24]. More recently, experimental results with Al [25] and especially Sc termination [26,27] look very promising, with large NEA values reported and with surfaces stable to high temperatures. Results suggest that for metals deposited directly onto the diamond surface, carbide-forming TMs give rise to more negative NEA values. Overall, results indicate that for optimal NEA, together with an air- and temperature-stable diamond surface, it is desirable for the adsorbate to have: (a) a high electropositivity, (b) a relatively small radius, (c) form stable bonds with both C and O, and (d) form stable highly charged positive ions.

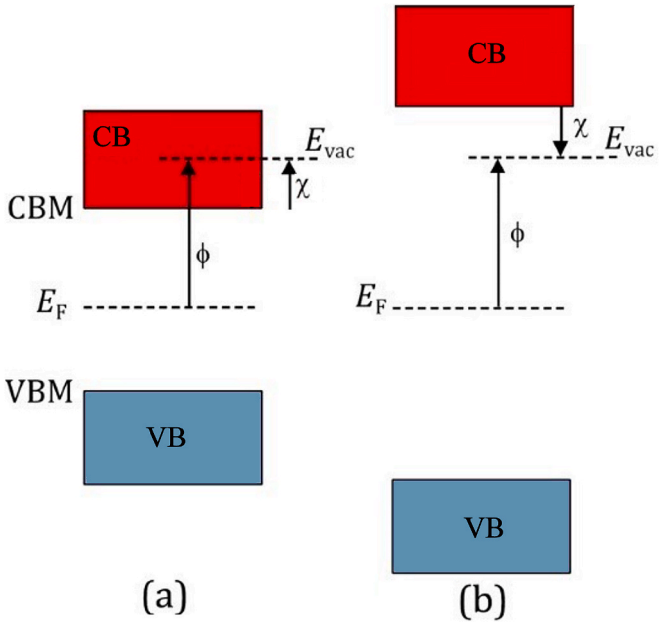

Fig. 1. Schematic diagram illustrating the electron affinity, χ, and the work function, ϕ, in relation to the Fermi level, E_F, and a fixed vacuum energy level, E_{vac}, for (a) a PEA and (b) an NEA semiconducting material. The valence band (VB) maximum energy is denoted as VBM, while the conduction band (CB) minimum energy is denoted as CBM.

Apart from metals, other adsorbate candidates that satisfy these criteria are the Group (4) elements silicon and germanium. A series of investigations by workers at La Trobe University explored terminating the (1 0 0) surface of diamond with up to 1 monolayer (ML) of Si. Experiment showed a (3 × 1) surface reconstruction following Si termination and annealing [28], with a reported NEA of −0.86 ± 0.1 eV [29–31]. Local-density approximated (LDA) DFT studies were also carried out on these systems, confirming the (3 × 1) surface as minimum-energy structure and predicting an NEA of −0.80 eV [32]. Germanium was also demonstrated experimentally to display an NEA of −0.71 ± 0.1 eV and give rise to a similar (3 × 1) surface reconstruction [33]. LDA DFT investigations of Ge adsorbed on the (100) surface support the (3 × 1) reconstruction geometry and predict an NEA of –0.85 eV.

As discussed previously, the origin of the NEA is attributed to the formation of the surface dipole due to adsorption of an electropositive adsorbate. Several schemes exist to analyse the magnitude of the charges on atoms in DFT, one of the most commonly used being Mulliken charges. However, a Mulliken analysis of the charges of atoms that are comprised of localised Gaussian basis sets is understood to be basis-set dependent, and very different charges can be assigned to the same atom for a given system depending on the basis set used. An alternative method of charge analysis was developed by Bader based on his quantum theory of atoms in molecules (QTAIM) [34]. Here, atoms are partitioned into so-called atomic basins which are bounded by interatomic surfaces, which, in the QTAIM formulism, defines the 'atoms' in the system of interest. For all points on this surface, the flux of the electron density is zero:

$$\mathbf{n}\cdot\nabla\rho(\mathbf{r}) = 0 \quad (2)$$

where $\mathbf{n}$ is the unit vector normal to the surface, and $\nabla\rho(\mathbf{r})$ is the gradient of the electron density, ρ, at position $\mathbf{r}$. The total charge of the atomic basin is then determined by integrating the density in the basin to calculate the total number of electrons assigned to the atom. The total number of electrons is then deducted from the atomic charge:

$$q\left(\Omega\right) = Z_\Omega - \int_\Omega \rho\left(\mathbf{r}\right)\mathrm{d}\mathbf{r} \quad (3)$$

where Z_Ω and $q(\Omega)$ are, respectively, the atomic and net charges of the atomic basin Ω. Any atomic property $P(\Omega)$, such as an atomic-basin dipole for a given atom, is obtained by calculating the expectation value of that property (using the relevant operator) over the basin Ω.

Another quantity that arises from a topological analysis of the electron density is the ellipticity, ε:

$$\varepsilon = (\lambda_1/\lambda_2) - 1 \quad (4)$$

where λ_1 and λ_2 are, respectively, eigenvalues of the Hessian of ρ at the bond critical point (BCP) along two orthogonal curvatures. By measuring the behaviour of the electron density via the ellipticity, one may assess the degree of π-character of the bond at the BCP. The larger the value of the ellipticity, the more anisotropic the electron density along these vectors and, in general, the greater the π-like nature of the bond. Note the distinction between the atomic basin dipole (ABD) calculated from the Bader analysis, *i.e.*, the dipole that exists about an individual atom within its own basin Ω, and the (planar) surface dipole due to the $M^{\delta+}$–$C_s^{\delta-}$ charge separation, to which we have already referred.

In order to determine the EA of a surface, the method of Fall *et al.* is often used [35]. Here, the calculated difference in energy between the valence band maximum (VBM) and the average electrostatic potential of *bulk* diamond is added to the average electrostatic potential of the surface under investigation. This results in the position of the VBM of the

surface. In order to determine the CBM, the bulk band gap, E_g, of diamond is then added to this VBM value. Frequently, the XC functionals involved in the calculation of E_g are either LDA or generalised gradient approximated (GGA). Approximations made at these levels of theory lead to a large underestimation of the E_g, providing an erroneous EA. Hence, in order to predict accurately the location of the CBM, LDA and GGA DFT studies utilise the experimental value of the diamond band gap, $E_{g,exp}$, thus turning an otherwise *ab initio* investigation into one that is semi-empirical. This problem can be mitigated by employing an XC functional that better predicts E_g. Functionals such as B3LYP – a hybrid functional that includes 20 % of the exact Hartree-Fock energy – significantly improves the calculation of E_g over GGAs, including that of diamond of course [36]. The *ab initio* program CRYSTAL17 [37] allows for the use of such functionals at only modest computational cost.

Here we present a DFT investigation of Si and Ge adsorption onto the bare (100) diamond surface using the *ab initio* software package CRYSTAL17. In this paper, the EA and adsorption energies (E_{ads}) are calculated using the hybrid XC functional B3LYP. This functional is also used to determine the band gap of bulk diamond, E_g, so that the EA is predicted with no need for the experimental value, $E_{g,exp}$. The surfaces are terminated with up to 1 monolayer (ML) of Si and Ge, and their structural, energetic, and electronic properties determined. Further details of the calculations can be found in the Supplementary Information (SI).

2. Methods

The CRYSTAL17 [37] *ab initio* software package was employed for all calculations. Bulk systems were modelled using three-dimensional periodic-boundary conditions. Surfaces were modelled using twelve-layer two-dimensional slabs produced by slicing the bulk diamond along the (100) crystallographic plane. In these slab systems, periodic-boundary conditions were applied to the surface in-plane vectors of the slab, *i.e.*, x and y coordinates only. All calculations were performed using the B3LYP hybrid exchange–correlation (XC) functional. The CRYSTAL17 program performs periodic calculations based on the linear combination of atomic orbitals (LCAO) approximation.

For all calculations, the Pople 6-21G [38] basis set was used for carbon. A similar basis set has been shown in the literature to provide an accurate description of diamond and its properties [39], and was found from our benchmarking analysis to reproduce bulk properties with good accuracy. Similar to the use of the expanded triple-zeta with polarisation (TZVP) basis set for defects within a 6-21G carbon bulk [40], we have employed pob-TZVP-rev-2 [41] for Si and Ge adsorbates. The values of program parameters ITOL1, ITOL2, ITOL3, ITOL4, and ITOL5, which control the Coulomb and exchange cut-offs, were respectively set to 7, 7, 7, 8, and 18. These values have also been used in the literature to model diamond slabs using CRYSTAL [18]. The SCF convergence tolerances were set to 10^{-8} Ha. A Monkhorst-Pack scheme was chosen for the sampling of k-points in the Brillouin zone. For all slabs investigated, an $8 \times 8 \times 1$ k-point sampling mesh was used. Slabs contained twelve layers of carbon atoms, because in preliminary investigations we found that twelve layers provided sufficient convergence with respect to the parameters of interest: the specific surface energy, the bond lengths in the slab core and surface, the surface band gap, and the work function. Each layer contained four carbon atoms. A full set of benchmarking calculations is given in the SI.

To determine the diamond lattice parameter used in slab calculations, bulk diamond supercells were optimised with respect to both the lattice constant and atomic positions. From this set of calculations, the converged values of the bulk lattice constant, C–C bond length, and band gap with respect to supercell size and the number of k-points were determined. Further, the energy separation between the C 1s orbital and the VBM was calculated. To construct the slabs, the converged lattice constant from these bulk calculations was used. For all slab calculations this value was held constant, *i.e.*, only the atom positions in the slabs were optimised.

The adsorption-configuration space was explored by initialising adsorbates onto different permutations of the high-symmetry surface structures of the (1 × 1) and reconstructed (2 × 1) bare (1 0 0) surface, as shown, respectively, in Fig. 2(a) and Fig. 2(b). For the (1 × 1) surface, these structures are defined as on-top (OT), pedestal (PE), bridge-A (BA), and bridge-B (BB). For the reconstructed (2 × 1) surface cell containing 8 atoms, these structures are termed pedestal (HH), bridge (HB), valley bridge (T3), and cave (T4). Adsorbates were positioned ~1.5 Å above these positions on both the upper and lower surfaces of the slab. Coverages of 1, 0.67, 0.5, and 0.25 ML – where 1 ML constitutes one adsorbate atom per surface C atom – were investigated. Multiple starting conformations were investigated.

The adsorption energy of an atom on a surface is defined as:

$$E_{ads} = (E_{total} - E_{slab} - NE_{at})/N \quad (5)$$

where E_{total} is the energy of the slab containing adsorbates, E_{slab} the energy of the substrate slab, E_{at} the energy of the isolated adsorbate, and N the number of adsorbates. To determine the electron affinities, the energy separation between the C 1s orbital and the VBM of the *bulk* supercell was added to the C 1s energy found for carbon atoms at the centre of the slabs. This provides the position of the VBM. To this VBM was added the bulk band gap calculated using the B3LYP XC functional, $E_{g,B3LYP}$, to determine the position of the CBM. This value was then referenced to E_{vac} of the slab, which was itself determined via a plane-averaged electrostatic-potential calculation [35]. This difference, as given in equation (1), provides the EA.

3. Results

We begin this section with an overview of the E_{ad} and EA values found for the conformationally stable structures of both adsorbates, noting any general trends observed. We then proceed to discuss several of the 0.25, 0.5 and 1 ML structures in more detail, comparing differences in the Mulliken and Bader charges, band structures, density of states (DOS), and bond critical points (BCPs).

Table 1 contains the $E_{ad,}$ EA, and surface work function, ϕ_s, values for each conformational energy minimum found for Si and Ge. The most exothermic adsorption energy for each adsorbate is found for a 0.67 ML coverage, in agreement with previous experimental and theoretical findings [28,32,33]. For Si and Ge, we determine these E_{ad} energies to be −7.35 eV atom^{-1} and −6.97 eV atom^{-1}, respectively. As anticipated from their Group-4 electronic configurations, a significant overlap is found between the structures accessible to both adsorbates. For 0.25 ML, both Si and Ge form HH, HB, T3, and T4 structures. For 0.5 ML, T4, HB, and T4 + HB ($\sqrt{2} \times \sqrt{2}$) are common to both adsorbates. Further, a 1 ML (1 × 1) structure is also found for both Si and Ge. In contrast, several structures are unique to one of the adsorbates, *e.g.*, a 0.5 ML HB + T4 linear and a dimer-bridging arrangement are found only for Si, while Ge displays half-monolayer HB + T4 ($\sqrt{2} \times \sqrt{2}$) and T4 ($\sqrt{2} \times \sqrt{2}$) surfaces in addition to a 1 ML (2 × 1) structure, none of which are found for Si.

Turning to the electron affinity, an NEA is found for every structure except for the Si 0.5 ML HB + T4 linear configuration, which displays a PEA of 0.57 eV. Besides a few exceptions, for a given elemental adsorbate, larger NEAs are generally found for larger adsorbate coverages. The largest NEA for Ge is found to be −3.33 eV for the 1 ML (2 × 1) structure, while the largest NEA for Si is determined to be −2.03 eV for the 0.5 ML HB surface. Further, we find that Ge displays a larger NEA than Si for every structure common to both elements.

3.1. 0.25 ML Si & Ge

Si and Ge have identical 0.25 ML configurations, shown in Fig. 3. The relative thermodynamic stability of these structures is the same for both elements: T4 > HB > T3 > HH. Ge displays higher exothermic

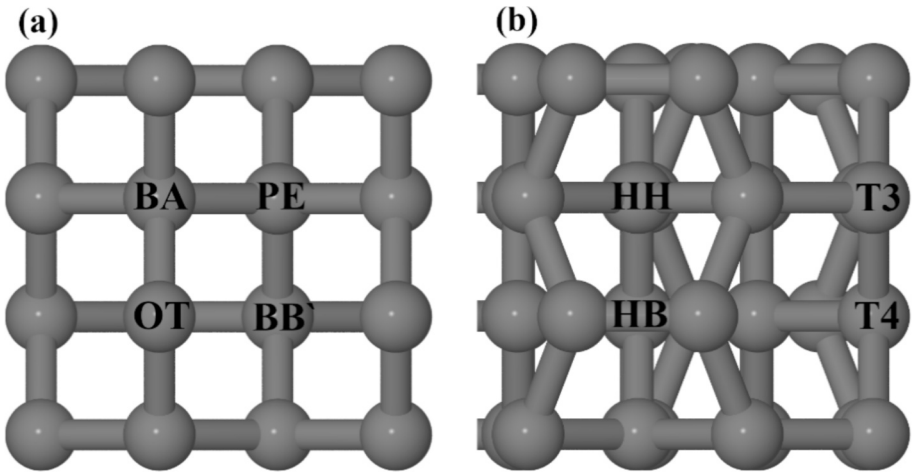

Fig. 2. Top-down images, viewed along the [100] direction, of the high-symmetry locations on the (a) (1 × 1), and (b) (2 × 1) reconstructed bare (100) diamond surface. Site labels are defined in the body text.

Table 1
Values of adsorption energy, E_{ad}, electron affinity, χ, and surface work function, ϕ_s, determined for Si and Ge adsorbate conformations.

Coverage / ML	Structure		E_{ad} / (eV atom^{-1})	χ / eV	ϕ_s / eV
0.25	Si	HH	−4.41	−0.43	5.14
		HB	−5.86	−0.62	5.09
		T3	−4.67	−0.81	4.71
		T4	−5.88	−0.31	5.29
	Ge	HH	−3.91	−0.93	4.33
		HB	−5.70	−1.46	4.38
		T3	−4.60	−1.42	3.70
		T4	−5.98	−1.20	4.52
0.5	Si	T4	−7.08	−1.42	4.54
		HB	−6.68	−2.03	4.08
		HB + T4 ($\sqrt{2} \times \sqrt{2}$)	−5.90	−0.61	5.44
		HB + T4 (linear)	−4.96	0.57	4.83
		Dimer bridge	−6.86	−1.62	4.44
	Ge	T4	−6.89	−2.13	3.86
		HH	−4.86	−2.11	4.08
		HB	−6.27	−2.58	3.70
		HB + T4 ($\sqrt{2} \times \sqrt{2}$)	−5.92	−1.74	4.38
		T4 ($\sqrt{2} \times \sqrt{2}$)	−5.81	−1.16	4.63
0.67	Si	(3 × 1)	−7.35	−1.71	4.35
	Ge	(3 × 1)	−6.97	−1.82	3.65
1	Si	(1 × 1)	−6.11	−0.15	3.82
	Ge	(1 × 1)	−5.63	−3.33	2.74
		(2 × 1)	−6.38	−2.10	3.61

adsorption energies. The Si and Ge T4 minimum-energy structures show similar E_{ads}: Si = –5.88 eV atom^{-1} and Ge = –5.98 eV atom^{-1}. With respect to adsorbate bonding to the underlying carbon surface, the configurations can be divided into those that are two-coordinate (T4 and HB), and those that are four-coordinate (T3 and HH). For a given structure common to both adsorbates, Ge displays significantly larger NEA values than Si. For Si we determine NEA values of T4 (–0.31 eV) < HH (–0.43 eV) < HB (–0.62 eV) < T3 (–0.81 eV), and for Ge the NEAs are HH (–0.93 eV) < T4 (–1.20 eV) < T3 (–1.42 eV) < HB (–1.46 eV). These data show that T4 and HH display the two smallest NEAs for both adsorbates, while the two largest NEAs are found for T3 and HB; for Ge these latter two structures differ in their NEAs by only 0.04 eV. No obvious relationship between structure stability and EA is evident from our data.

Table S1 in the Supplementary Information contains Mulliken and Bader charges for the adsorbate, surface carbons, and second-layer carbons in each of the 0.25 ML surfaces. For a given structure, Mulliken and Bader charge partitioning yield significantly different results, even though in both schemes, adsorbate charges are found to be positive, as anticipated by the more electropositive nature of Si and Ge compared to C.

Mulliken charges for a given adsorbate are found to be similar in every configuration: Si charges are in the range 0.34 – 0.53 *e*, while Ge charges span 0.48 – 0.73 *e*. For Si, the ordering of the Mulliken charge for each surface is HB < HH < T4 < T3, and for Ge a similar trend HB < T4 < HH < T3 is found. For identical structures, Ge is found to have a higher positive charge than Si by ~0.1 – 0.3 *e*.

The results above contrast with those found in a Bader analysis. Here, the magnitude of the positive charge is found to be larger for both adsorbates in every structure compared to those found from the Mulliken analysis. For Si, adsorbate charges are 1.67 *e* (HH) > 1.38 *e* (T3) > 1.19 *e* (HB) > 1.14 *e* (T4). For Ge, an identical ordering is found: 1.08 *e* (HH) > 1.02 *e* (T3) > 0.82 *e* (T4) > 0.80 *e* (HB). These results show that, under the Bader scheme, Si displays higher positive charges than Ge.

Differences are also found in the two methods of analysis for the charges on carbon. Mulliken charges for C in the surface and second layers are found to alternate significantly. This is not surprising as orbital-based methods have been shown to have a much larger dependence on basis set than electrostatic potential and volume-based methods [42]. On the surface C layer, both negative and positive charges are found, the latter being typically small in magnitude, *e.g.*, ~ |0.0 – 0.1| *e*. Charges on C in the second layer are frequently larger in magnitude than those on the surface, *e.g.*, ~ |0.1 – 0.2| *e*. This highlights a key feature found in the Mulliken charge partitioning; non-negligible charge attributed to C is found to permeate 3–4 layers into the slab. These charge alternations mean that it is not straightforward to form an approximate planar $M^{\delta+}$–$C_s^{\delta-}$ dipole model of the surface between either Si or Ge and the surface carbon layer. Such alternations have been noted previously in other (conjugated) carbon chains and criticised as unphysical [43]. With Bader partitioning, however, we observe that the majority of the electron density lost from the adsorbate is distributed on the surface carbons. Charges within this layer are ~−0.2 to −0.6 *e*. We emphasise here that all charges within the surface layer are negative, in contrast to those from the Mulliken scheme, and are much larger in magnitude. Carbon atoms in the second layer are found to have lower Bader charges, e.g., ~ |0.0 – 0.2| *e*. Indeed, charge alternations of C atoms going into the slab are significantly reduced. Because of this confinement of the majority of the charge transfer to the adsorbate (which becomes positively charged) and the surface carbons (which become negatively charged) a surface dipole can be calculated.

Table S3 in the SI contains the adsorbate-C_s bond critical point (BCP) data for each 0.25 ML structure. We compare these BCP data to values

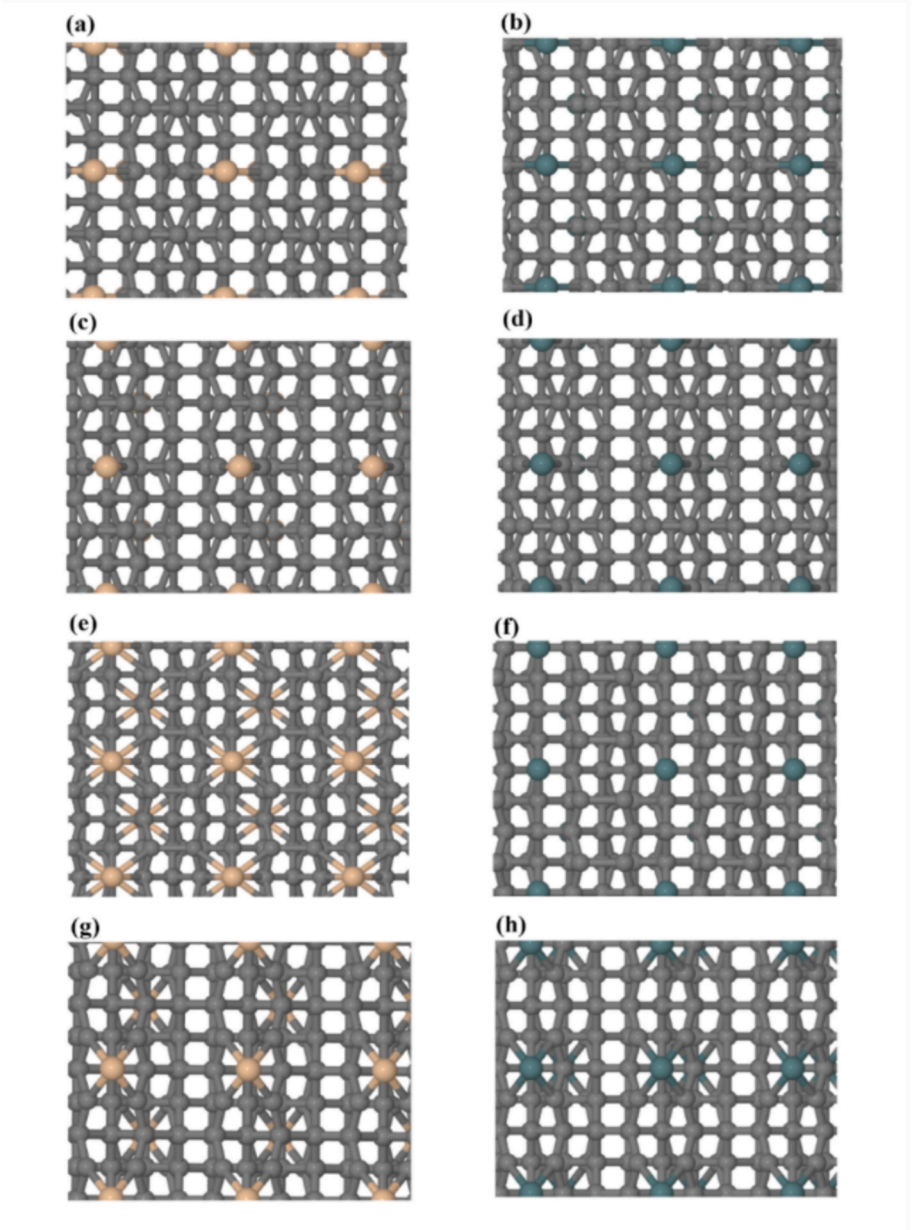

Fig. 3. Top-down images of the 0.25 ML configurations of Si (left column) and Ge (right column) showing (a)-(b) T4, (c)-(d) HB, (e)-(f) T3, and (g)-(h) HH configurations. Si atoms are beige, Ge green.

found for the bulk-like C–C bonds in the central region of the slabs, which are considered ideal σ covalent bonds. Here, the density, Laplacian, and ellipticity are found to be 0.23 au, −0.54 au, and 0.00, respectively. These data show a high concentration of density at the C–C BCP that is locally concentrated at the BCP and is of σ character. The electron density at M−C BCPs varies between 0.07 and 0.10 au for Si and 0.06 – 0.10 au for Ge. Both Si and Ge share a similar trend in the ordering of the magnitude of the density for each configuration; Si: T3 < HH = T4 < HB; Ge: T3 < HH < T4 < HB. These data suggest larger electron densities, *i.e.*, greater covalency, at the BCPs of the two-coordinate surfaces HB and T4. Distinct differences, however, are found in the Laplacian and ellipticity at BCPs of the different coordination sites. In the HH and HB surfaces much larger values are found for these two quantities. The values of the Laplacian at these sites for both elements are similar; Si 0.13 (HB) and 0.11 au (HH); Ge 0.11 (HB) and 0.12 au (HH). The small positive values indicate that, at the M−C_s BCPs for HB and HH surfaces, ρ is locally weakly depleted, thus suggesting polar-covalent M−C_s bonds. For Si and Ge T3 and T4 sites, the Laplacian is close to zero, indicating a smoothly varying density. The ellipticity varies more for Si (0.07 – 0.71) than Ge (0.09 – 0.34), with larger values found at BCPs at the HB and HH sites. Hence, these data show a larger degree of anisotropy in the electron density at the HB and HH coordination sites, suggesting some degree of π-like bonding character at these sites.

For a given configuration, the electronic (band) structures for the two adsorbates are almost identical (see band structure diagrams Figs. S1 and S2 in the SI). Each diagram displays empty low dispersion states in the band gap. For HB structures, empty band-gap states display particularly low dispersions, indicating that the states are highly localised. Inspection of the DOS projected onto the adsorbate and carbon layers (Figs. S3 and S5 in the SI), show that filled states in the vicinity of the VBM tend to contain their largest contributions from the adsorbate and surface C atoms. The two-coordinate nature of the T4 and HB surfaces lead us to anticipate occupied and localised adsorbate states for both structures, reflecting non-bonded electrons situated on the

adsorbates. Indeed, the T4 and HB DOS show a set of states largely located on the adsorbates with minor contributions from the surface carbons. The projected density-of-states (PDOS) for the adsorbates (Figures S4 and S6 in the SI) show that these occupied adsorbate states for T4 and HB in the vicinity of the VBM are formed primarily from orbitals of p_z symmetry and contain minor contributions from *s*-symmetry orbitals. These combinations imply sp_z hybridisation, which in turn suggests electrons projecting from the surface. As stated above, the four-coordinate T3 and HH structures contain occupied states in the vicinity of the VBM which are also formed from contributions of surface carbons and adsorbates. Here, however, in contrast to the two-coordinate systems, the states are primarily based on the surface carbons. Further, the PDOS for T3 and HH show that the contributions arising from the adsorbates are attributed primarily to p_x and p_y, which is expected, considering the surface symmetry, of the C_s–M bonds.

Differences between the electron-density distribution in the region of the adsorbate for the two- and four-coordinate structures can be seen in their electron-density and density-difference maps, where the difference density is relative to the superposition of the isolated atom densities. These are shown for the Ge T3 (four-coordinate) and T4 (two-coordinate) structures in Fig. 4(a) and 4(b), and Fig. 4(c) and 4(d), respectively. The density maps for the remaining surfaces are provided in Figs. S7, S8, and S9 in the SI. Together these show significant differences in the polarisation of the electron density for the two- and four-coordinate systems. In T4, there is a redistribution of electron density to regions vertically above Ge. The same observation is true for HB Ge, and T4 and HB Si. This contrasts with the reduction in the density in the same regions for both adsorbates in the four-coordinate T3 and HH structures. Although these four-coordinate surfaces display similar redistributions, a careful inspection of the HH structures shows a larger polarisation of density vertically above and close to the adsorbate. This is larger for Ge than Si as seen in the atomic-basin dipole (ABD) data (Table 2). For both adsorbates in all locations, there is a negative atomic-dipole-moment component parallel to the *z*-axis (along [100]), equal in magnitude to the total atomic-dipole moment within that atomic basin, *i.e.*, the atomic dipole points towards the surface from the vacuum and is almost entirely perpendicular to the surface plane. The negative value along the *z*-direction indicates a negative charge, *i.e.*, an electron distribution, in the vacuum region above each adsorbate. The order of the magnitude of each dipole for both adsorbates is identical: T3 < HH < T4 < HB, which reinforces our discussion of the density redistribution; for T4 and HB (two-coordinate) structures, where density is redistributed above the adsorbates, larger negative atomic dipoles are found. Conversely, for the T3 and HH (four-coordinate) configurations, where density is redistributed away from the vacuum region of the adsorbate, there are smaller negative atomic dipoles. The more negative dipole for HH over T3 for each adsorbate may relate, as discussed above, to the slight polarisation of density just above the adsorbate in the HH structure. Also, despite the significantly higher positive charges acquired overall by Si compared to Ge in all equivalent environments, for a given

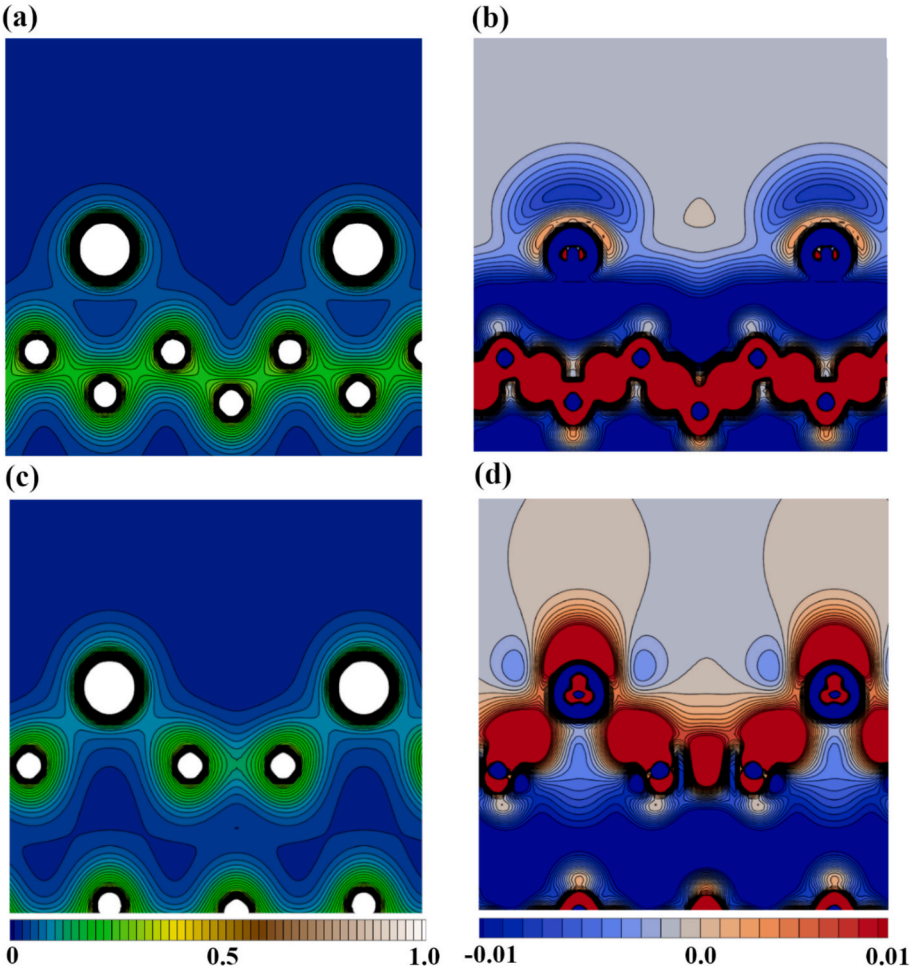

Fig. 4. Electron-density maps (left column) and electron-density-difference (right column) maps of the Ge 0.25 ML (a)-(b) T3 and (c)-(d) T4 structures. The images show a 2-D slice along the [110] direction. The Ge atoms are the two larger atoms at the top of each frame. Units are electron bohr^{-3}. Isodensity contours for electron–density maps differ by 0.01 electron bohr^{-3}, while in difference maps contours are separated by 0.001 electron bohr^{-3}. In all such plots, red denotes regions of increased electron density (electron accumulation) and blue regions of decreased electron density (electron depletion).

Table 2
Adsorbate atomic-basin dipole (ABD) moments determined using Bader's QTAIM theory. Note that the ABD moment is that directed along the [100] direction, *i.e.*, the negative value indicates that the dipole points from the vacuum towards, and perpendicular to, the surface of the slab.

Coverage / ML	Adsorbate	Structure	ABD moment / au
0.25	Si	HH	−1.59
		HB	−2.01
		T3	−1.03
		T4	−1.79
	Ge	HH	−1.24
		HB	−1.44
		T3	−0.81
		T4	−1.28
0.5	Si	T4	−1.35
		HB	−1.62
		HB + T4 ($\sqrt{2} \times \sqrt{2}$)	−1.96 (HB); −1.91(T4)
		HB + T4 (linear)	−1.72 (HB); −1.70 (T4)
	Ge	T4	−0.91
		HH	−1.16
		HB	−1.08
		HB + T4 ($\sqrt{2} \times \sqrt{2}$)	−1.36 (HB); −1.35 (T4)
		T4 ($\sqrt{2} \times \sqrt{2}$)	−1.38
1	Si	(1 × 1)	−1.59
	Ge	(1 × 1)	−1.07
		(2 × 1)	−0.82

configuration the *atomic* dipole moment of Si in its atomic basin is more negative than Ge, and in this context we note the larger NEAs displayed by Ge.

3.2. 0.5 ML Si & Ge

Si and Ge each display five 0.5 ML configurations, three of which are common to both adsorbates: HB, T4, and HB + T4 ($\sqrt{2} \times \sqrt{2}$). Additionally, Si independently displays a HB + T4 linear, and Ge a T4 ($\sqrt{2} \times \sqrt{2}$) structure. Images for these surface configurations appear in Figs. S10 and S11 in the SI. The Si dimer bridge and Ge HH surfaces are omitted from the following discussion.

Adsorption energies are, in general, more exothermic for 0.5 ML surfaces than for 0.25 ML surfaces. As with the 0.25 ML structures, the exothermicity of adsorption in the T4 location for 0.5 ML is higher than that found at HB; the most thermodynamically stable half-monolayer configuration for both adsorbates is the T4 surface (Si: –7.08 eV atom^{-1}; Ge: –6.89 eV atom^{-1}). Combinations of HB and T4, such as the Si and Ge HB + T4 ($\sqrt{2} \times \sqrt{2}$) and the Si linear HB + T4, display reduced exothermicity compared to structures that involve the adsorbate exclusively in the HB or T4 position. In general, the NEA of Ge > Si. The NEA for both 0.5 ML Si and Ge HB is larger than T4, which is also observed for the quarter monolayer. Structures produced from combinations of HB and T4, such as the Si surfaces HB + T4 ($\sqrt{2} \times \sqrt{2}$) and HB + T4 linear, either have less negative EAs (the former) or a PEA (the latter).

Comparison of the Mulliken and Bader charges for the 0.5 ML surfaces (Table S1 in the SI) reveals a similar pattern for the 0.25 ML structures. The Mulliken scheme again assigns larger positive charges to Ge than Si for the configurations T4, HB, and HB + T4 ($\sqrt{2} \times \sqrt{2}$). Further, significant charge alternations for C atoms penetrating several layers into the slab are found in the Mulliken analysis. Bader partitioning, instead, again shows the magnitude of all adsorbate positive charges to be larger than that from the Mulliken scheme, and Si acquires higher positive charges than Ge. Also, the Bader scheme indicates that the majority of the electron transfer from the adsorbate is confined to the surface C_s. Only small charges are attributable to C atoms in deeper layers.

For 0.5 ML structures, we observe that the adsorbate Bader charges of the HB and T4 surfaces are smaller than those of the analogous quarter-monolayer surface in which the adsorbate occupies the same bonding site. In half-monolayer surfaces, all C_s atoms and adsorbates are, respectively, equivalent, and the ratio of C_s to M is 2:1. Hence, all C_s atoms equally withdraw density from two adsorbates. For 0.25 ML surfaces, the ratio of C_s to M is 4:1, and there are two inequivalent sets of C_s sites; one that constitutes carbons that are bonded to M, and the other which constitute carbons in dimers that are not bonded to an adsorbate. Carbons in the former of these are able to withdraw density from the adsorbates like the 0.5 ML case, and are also in the same ratio (2:1). In addition, however, carbons in the latter set of sites, which have a C_s-to-M ratio of 2:1, additionally withdraw a small amount of electron density from M. Overall, in the quarter-monolayer surfaces HB and T4, adsorbates lose more density and acquire larger positive charges. Despite this, however, the larger number of adsorbates per unit surface area in half-monolayer T4 and HB surfaces results in a larger planar $M^{\delta+}$–$C_s^{\delta-}$, which is consistent with their generally larger NEAs compared to 0.25 ML coverages.

In common with the observations made for the 0.25 ML surfaces, Ge continues to display both smaller planar $Ge^{\delta+}$–$C^{\delta-}$ dipoles but larger NEAs when compared to analogous 0.5 ML Si structures. The Bader charges acquired by Ge are, again, found to be significantly smaller than those of Si. For instance, for Ge on the 0.5 ML HB surface a charge of 0.58 *e* and NEA of –2.58 eV are observed compared to the respective values of 1.05 *e* and –2.03 eV for the analogous Si HB surface.

Band structures of the 0.5 ML Si and Ge surfaces (Figs. S12 and S13 in the SI) reveal that the HB, T4, and ($\sqrt{2} \times \sqrt{2}$) combination thereof are semiconducting, and contain empty low-lying states. The Si HB + T4 linear structure (Fig. S12(c) in the SI) is metallic. The DOS and PDOS of this latter surface (Figs. S14(c) and S15(c) in the SI) show that these states in the vicinity of the Fermi level are mostly attributable to silicon p_x and p_y orbitals. The 0.5 ML Ge structures are all observed to be semiconducting (Fig. S13 in the SI). Indeed, the Ge HB and T4 band diagrams appear almost identical to their Si counterparts, as do their DOS and PDOS.

A topological analysis of the density (Table S4 in the SI) finds M−M, *i.e.*, adsorbate–adsorbate, BCPs for only the HB and T4 half-monolayer surfaces of Si and Ge. While it is immediately clear that no adsorbate–adsorbate bonding should be found for the Ge T4 ($\sqrt{2} \times \sqrt{2}$) surface or the HB + T4 ($\sqrt{2} \times \sqrt{2}$) surfaces of both elemental adsorbates due to the large lateral separation of adsorbate atoms (Ge T4 ($\sqrt{2} \times \sqrt{2}$) = 3.59 Å; Ge HB + T4 ($\sqrt{2} \times \sqrt{2}$) = 3.58 Å; Si HB + T4 ($\sqrt{2} \times \sqrt{2}$) = 3.59 Å), the same cannot be said for the Si HB + T4 linear configuration. Here, the Si–Si separation is 2.54 Å; the same as those at the Si HB and T4 surfaces, each of which do contain Si–Si BCPs (*cf.* Si–Si bond lengths of 2.35 Å in crystalline). However, the absence of Si–Si bonds in the HB + T4 linear surface is not surprising considering the orientation of the electron distribution that would be required around Si. To form two bonds to adjacent Si atoms, a significant distortion of the typical sp^3 tetrahedral electron distribution would be required, so that the electrons participating in the Si–Si bonds would lie in the same plane as those electrons in the Si–C bonds. This would be energetically highly unfavourable. Indeed, absence of bonds between Si atoms in the HB + T4 linear structure is evident in the density-difference plot in Figure S18(f) in the SI, where there is a polarisation of the density away from the inter-Si regions. This is clearly quite different than the situation with HB and T4 Si (Figures S18(b) and S18(d) in the SI), and HB and T4 Ge (Figs. S19 (b) and S19(d) in the SI), where there is polarisation of density into regions between adjacent adsorbates. With respect to their M−C BCPs (Table S3 in the SI), little variation is found in the density and Laplacian between the HB and T4 surfaces with that analysed for the quarter monolayer. The ellipticity, however, can be seen to reduce for both Si and Ge when moving to 0.5 ML coverages. This is most marked for Si, where values of 0.46 and 0.02 are found for the HB and T4 0.5 ML surfaces, respectively, compared to 0.71 and 0.21 for 0.25 ML coverages in the same binding location. For the HB and T4 surfaces of both elements, little distinction is found between the density and Laplacian of the 0.5 ML M−M BCPs (Table S4 in the SI). The ellipticity does appear,

however, to be larger for both elements in the HB configuration.

The above discussion implies that Si and Ge adsorbates in the HB and T4 surfaces are fully valent, in that each adsorbate forms four bonds. The other 0.5 ML surfaces discussed above, in contrast, may be expected to contain lone pairs, dangling bonds, or double bonds due to their unfulfilled valence. The presence of non-bonded electrons manifests itself in the atomic-basin dipole data in Table 2. For Si HB + T4 linear and HB + T4 ($\sqrt{2} \times \sqrt{2}$), and Ge T4 ($\sqrt{2} \times \sqrt{2}$) and HB + T4 ($\sqrt{2} \times \sqrt{2}$), ABD moments are, for a given location, more negative than those of either 0.5 ML HB or T4 for a given elemental adsorbate. These values suggest that, while valence electrons in HB and T4 project less from the surface, these other 0.5 ML structures contain valence electrons that project further into the vacuum. Further, as with the quarter monolayer surfaces, 0.5 ML Ge, despite displaying smaller Bader charges and thus smaller $M^{\delta+}$–$C_s^{\delta-}$ surface dipoles, continues to provide smaller, *i.e.*, less negative, ABDs over Si considering the like-for-like structures T4 and HB. This may again explain, similar to the 0.25 ML surfaces, the larger NEAs displayed by Ge.

3.3. 1.0 ML Si & Ge

At 1 ML coverage, Si displays only a single structure while Ge displays two. These surfaces are shown in Figure S20 in the SI. Both elements share a common 1 ML (1 × 1) structure in which the adsorbates form a (1 0 0)-like diamond plane on top of an unreconstructed (1 × 1) diamond surface. Ge additionally acquires an arrangement in which the underlying C surface is (2 × 1), with Ge occupying sites almost vertically above the C surface dimers. This latter structure displays the largest E_{ads} (–6.38 eV atom^{-1}), followed by Si (1 × 1) (–6.11 eV atom^{-1}) and Ge (1 × 1) (–5.63 eV atom^{-1}). Continuing the trend observed in smaller coverages, we find the Ge surfaces to have larger NEAs than the Si structure: Ge (1 × 1) = –3.33 eV > Ge (2 × 1) = –2.10 eV > Si (1 × 1) = –0.31 eV.

An analysis of the Mulliken and Bader charge distributions for these surfaces demonstrates the same pattern observed for smaller coverages. In the Mulliken scheme, smaller positive charges are found for Si than Ge in shared (1 × 1) structures, and charge alternates on the C atoms several layers into the slab (Table S2 in the SI). In contrast to the Mulliken populations, Bader partitioning again attributes larger positive charges to all adsorbates, and larger positive charges are associated with Si than Ge. We continue to find a reduction in the charge-per-adsorbate relative to adsorbate charges at smaller coverages. However, the overall surface $M^{\delta+}$–$C_s^{\delta-}$ dipoles are larger for 1 ML coverage due to the increased adsorbate density. The NEA of –3.33 eV calculated for this surface is also the largest NEA of all the Ge structures. In contrast, although the $Si^{\delta+}$–$C_s^{\delta-}$ surface dipole is also the largest of all Si structures in this work, the associated NEA of –0.15 eV is extremely small. Although the magnitude of the atomic dipole of Si within its atomic basin is fairly large (–1.59 au), more negative atomic-dipole moments for Si exist for lesser coverages that have larger NEAs, *e.g.*, 0.25 ML HB and T4, and 0.5 ML HB. However, we note that the 1 ML (1 × 1) surface has more Si atomic-basin dipoles due to the increased areal density of Si compared to these 0.25 and 0.5 ML structures. Hence, the increased number of these atomic Si dipoles may suppress the NEA of the 1 ML surface.

Band structures for the three 1 ML surfaces are provided in Figure S21 in the SI. All surfaces are shown to be metallic and contain a large number of highly dispersed, *i.e.*, delocalised, states that span the surface band gap. For Si and Ge (1 × 1), the Fermi level resides approximately in the middle of the band gap. For the Ge (2 × 1) surface, the Fermi level resides close to the VBM. For the (1 × 1) structures of both elements, these band-gap states can be seen from DOS in Fig. S22 (a)-(d) in the SI to originate from approximately equal contributions from the adsorbate and surface carbons. An inspection of the adsorbate PDOS plots shows that these gap states originate from *s*, p_x, and p_y orbitals of similar weighting. Hence, these likely reflect empty C_s–M states. In contrast, the Ge (2 × 1) structure demonstrates band-gap states that are almost entirely attributable to Ge *s*, p_x, and p_y orbitals with almost no contribution from the surface carbons, implying empty Ge–Ge states.

Significant differences are also observed in the electron-density plots (Fig. S22 in the SI) and the M−M BCP data (Table S4 in the SI) for the (1 × 1) and (2 × 1) surfaces. In the former, the density-difference plots for both elemental adsorbates within the plane of the adsorbate layer show a polarisation of density between adjacent adsorbates along only a single direction. Corroborating this, an inspection of the critical points for these (1 × 1) surfaces indicates that BCPs are present only between adsorbates along orientations in which electron density accumulates. The Ge (2 × 1) surface is quite different, however. In the density-difference plot, a polarisation of density is seen between Ge adsorbates along two perpendicular directions. A BCP analysis of this (2 × 1) surface indicates four Ge–Ge BCPs per adsorbate are present: two along the [110] direction, and two along the $[\bar{1}10]$ direction. In the former, BCPs are shown to be equivalent. Along the latter $[\bar{1}10]$ direction, however, two similar but inequivalent BCPs are found between adjacent Ge adsorbates above the surface C–C dimer and also above Ge–Ge bridging C–C dimer rows.

4. Discussion, conclusions, and future work

It is interesting to highlight the larger NEA values exhibited by Ge, despite it displaying smaller adsorbate charges and thus smaller planar surface dipoles. This is even more intriguing given that both Ge and Si have the same valency, and also demonstrate similar adsorbate–adsorbate and adsorbate-C bonding arrangements and properties. However, as highlighted in earlier sections, significant differences are found with respect to the ABD moments of the two elements. For nearly all structures within a coverage subset, Si displays more negative atomic-dipole moments than Ge. This indicates that, despite having fewer electrons in the atomic basins of Si, the electrons which are present project to a greater extent from the surface towards the vacuum. This may indicate that, in addition to the surface planar dipole as a first-order approximation to the determination of the NEA, a higher-order factor relating to the electron density in the adsorbate atomic basin would lead to a predictive model for the EA, in which more negative ABDs may correlate with a smaller NEA for a given $M^{\delta+}$–$C_s^{\delta-}$ planar dipole.

In order to consider other factors that affect the NEA, a further evaluation of the structures that display 'anomalous' NEA values – namely, Si 0.5 ML HB + T4 linear, Si 0.5 ML HB + T4 ($\sqrt{2} \times \sqrt{2}$), and 1 ML Si (1 × 1) – is warranted. For the first of these, the most obvious difference between this and other 0.5 ML surfaces is the large number of C–C dimer bonds exposed to the vacuum. These C atoms display a small negative charge of –0.08 *e*. Coupled with this is the high electron density situated in the dimer due to the presence of the π bond. The PEA displayed by this surface may be explained by the presence of both lone pairs situated on Si and the π electrons situated in the C–C dimer. An anomalous feature of the Si 1 ML (1 × 1) surface is the very high value of the ellipticity found in a Bader analysis of the Si–Si BCPs. This value of 0.34 is significantly larger than the value of 0.05 found for the analogous 1 ML Ge (1 × 1) surface.

Finally, the exposed dangling bonds on the 0.25 ML and 0.5 ML structures clearly make further oxidation/hydrogenation/chemical-attack facile. The high coordination number of Si in the 1 ML surface may confer stability over the lesser coverages with respect to chemisorption, but exposure to atmosphere may still result in oxidation or hydrogen addition which may alter the EA and render a device failure. Conversely, dangling bonds may afford an opportunity to modify the surface further and enhance functionality.

In conclusion, attachment of Si and Ge to a (1 0 0) diamond surface leads to a NEA when directly adsorbed onto the bare carbon surface. Si adsorbates display surfaces which tend to provide more exothermic adsorption energies, but Ge adsorbates demonstrate larger NEAs.

However, despite displaying larger NEAs, the surface Ge dipoles are smaller than that for Si. In this context, we note that Ge adsorbates display less negative atomic-basin dipoles, which may explain the tendency of the Ge-adsorbed surfaces to display larger NEAs. Agreement with experiment is reasonable but discrepancies remain, such as the differences between theory and experiment for 0.67 ML (3 × 1)-terminated Si and Ge surfaces. Experimental values of 0.86 ± 0.1 eV for Si, −0.71 ± 0.1 eV for Ge) compare with calculated values of − 1.71 eV and − 1.82 eV, respectively. More work is needed to see whether this is due to the use of hybrid DFT, differences in surface structure, or a limitation of surface supercell size.

We plan further studies in which the elements Li, Mg, and Al are adsorbed on the (1 0 0) diamond surface, examining the surface dipoles and ABDs, calculated using Bader partitioning as well as their NEA values. These studies will generate significant additional data in which Group (1) (Li), Group (2) (Mg), and Group (3) (Al) elemental adsorbates – in addition to the Group (4) elements covered in this work – can be compared and contrasted in detail, and provide more opportunities to establish correlation between EA values and the structure, dipole moments and bonding of different configurations.

CRediT authorship contribution statement

Neil L. Allan: Writing – review & editing, Validation, Supervision, Project administration, Funding acquisition, Formal analysis, Data curation, Conceptualization. **Paul W. May:** Writing – review & editing, Supervision, Investigation, Funding acquisition, Conceptualization.

Declaration of competing interest

The authors declare the following financial interests/personal relationships which may be considered as potential competing interests: Paul May reports financial support was provided by Engineering and Physical Sciences Research Council. Paul May reports a relationship with Engineering and Physical Sciences Research Council that includes: funding grants. If there are other authors, they declare that they have no known competing financial interests or personal relationships that could have appeared to influence the work reported in this paper.

Acknowledgements

The authors thank Adam Kirwan who performed much of the DFT simulation work and wrote the first draft of this paper. We also acknowledge funding from the UK Engineering and Physical Sciences Research Council (EPSRC), United Kingdom via the Diamond *Science and Technology* Centre for Doctoral Training (Grant number: EP/L015315/1). This work was carried out using the computational facilities of the Advanced Computing Research Centre, University of Bristol (http://bris.ac.uk/acrc/).

Appendix A. Supplementary data

Supplementary data to this article can be found online at https://doi.org/10.1016/j.apsusc.2025.164732.

Data availability

Data will be made available on request.

References

[1] P.W. May, Diamond thin films: a 21st century material, Phil. Trans. R. Soc. Lond. A 358 (2000) 473–495, https://doi.org/10.1098/rsta.2000.0542.
[2] P.W. May, R. Zulkharnay, Diamond thin films: A 21st century material. Part 2: A new hope, Phil. Trans. Roy. Soc. Lond. A 383 (2025) 20230382, https://doi.org/10.1098/rsta.2023-0382.
[3] R. Zulkharnay, P.W. May, Applications of diamond films: a review, Funct. Diamond 4 (2024) 2410160, https://doi.org/10.1080/26941112.2024.2410160.
[4] M.C. James, F. Fogarty, R. Zulkharnay, N.A. Fox, P.W. May, A review of surface functionalisation of diamond for thermionic emission applications, Carbon 171 (2021) 532–550, https://doi.org/10.1016/j.carbon.2020.09.019.
[5] E. Monroy, F. Omnes, F. Calle, Wide-bandgap semiconductor ultraviolet photodetectors, Semicond. Sci. Technol. 18 (4) (2003) R33–R51, https://doi.org/10.1088/0268-1242/18/4/201.
[6] P. Ascarelli, E. Cappelli, F. Pinzari, M.C. Rossi, S. Salvatori, P.G. Merli, A. Migliori, Secondary electron emission from diamond: physical modeling and application to scanning electron microscopy, J. Appl. Phys. 89 (1) (2000) 689–696, https://doi.org/10.1063/1.1326854.
[7] A. Shih, J. Yater, P. Pehrsson, J. Butler, C. Hor, R. Abrams, Secondary electron emission from diamond surfaces, J. Appl. Phys. 82 (4) (1997) 1860–1867, https://doi.org/10.1063/1.365990.
[8] F.A.M. Koeck, R.J. Nemanich, A. Lazea, K. Haenen, Thermionic electron emission from low work-function phosphorus doped diamond films, Diamond Relat. Mater. 18 (5) (2009) 789–791, https://doi.org/10.1016/j.diamond.2009.01.024.
[9] P. Strobel, M. Riedel, J. Ristein, L. Ley, O. Boltalina, Surface transfer doping of diamond by fullerene, Diamond Relat. Mater. 14 (3) (2005) 451–458, https://doi.org/10.1016/j.diamond.2004.12.051.
[10] D.B. Go, J.R. Haase, J. George, J. Mannhart, R. Wanke, A. Nojeh, R.J. Nemanich, Thermionic energy conversion in the twenty-first century: advances and opportunities for space and terrestrial applications, Front. Mech. Eng. 3 (2017), https://doi.org/10.3389/fmech.2017.00013.
[11] M.C. James, P.W. May, N.L. Allan, *Ab initio* study of negative electron affinity from light metals on the oxygen-terminated diamond (111) surface, J. Phys: Cond Matter 31 (29) (2019) 295002, https://doi.org/10.1088/1361-648X/ab18ef.
[12] K.M. O'Donnell, T.L. Martin, N.A. Fox, D. Cherns, *Ab initio* investigation of lithium on the diamond C(100) surface, Phys. Rev. B 82 (11) (2010) 115303, https://doi.org/10.1103/PhysRevB.82.115303.
[13] K.M. O'Donnell, T.L. Martin, M.T. Edmonds, A. Tadich, L. Thomsen, J. Ristein, C. I. Pakes, N.A. Fox, L. Ley, Photoelectron emission from lithiated diamond, physica status solidi (a) 211 (10) (2014) 2209–2222, https://doi.org/10.1002/pssa.201431414.
[14] M.C. James, A. Croot, P.W. May, N.L. Allan, Negative electron affinity from aluminium on the diamond (1 0 0) surface: a theoretical study, J. Phys: Cond Matter 30 (23) (2018) 235002, https://doi.org/10.1088/1361-648X/aac041.
[15] R. Zulkharnay, N.L. Allan, P.W. May, *Ab initio* study of negative electron affinity on the scandium-terminated diamond (100) surface for electron emission devices, Carbon 196 (2022) 176–185, https://doi.org/10.1016/j.carbon.2022.04.067.
[16] H. Pinto, R. Jones, D.W. Palmer, J.P. Goss, A.K. Tiwari, P.R. Briddon, N.G. Wright, A.B. Horsfall, M.J. Rayson, S. Öberg, First-principles studies of the effect of (001) surface terminations on the electronic properties of the negatively charged nitrogen-vacancy defect in diamond, Phys. Rev. B 86 (4) (2012) 045313, https://doi.org/10.1103/PhysRevB.86.045313.
[17] P. Rivero, W. Shelton, V. Meunier, Surface properties of hydrogenated diamond in the presence of adsorbates: a hybrid functional DFT study, Carbon 110 (2016) 469–479, https://doi.org/10.1016/j.carbon.2016.09.050.
[18] M. De La Pierre, M. Bruno, C. Manfredotti, F. Nestola, M. Prencipe, C. Manfredotti, The (100), (111) and (110) surfaces of diamond: an *ab initio* B3LYP study, Molec. Phys. 112 (7) (2014) 1030–1039, https://doi.org/10.1080/00268976.2013.829250.
[19] K.P. Loh, J.S. Foord, R.G. Egdell, R.B. Jackman, Tuning the electron affinity of CVD diamond with adsorbed caesium and oxygen layers, Diamond Relat. Mater. 6 (5) (1997) 874–878, https://doi.org/10.1016/S0925-9635(96)00737-6.
[20] J.L. Nie, H. Xiao, X.T. Zu, F. Gao, First principles calculations on Na and K-adsorbed diamond(100) surface, Chem. Phys. 326 (2006) 308–314, https://doi.org/10.1016/j.chemphys.2006.02.005.
[21] J. van der Weide, R.J. Nemanich, Schottky barrier height and negative electron affinity of titanium on (111) diamond, J. Vac. Sci. Technol. B 10 (4) (1992) 1940–1943, https://doi.org/10.1116/1.586162.
[22] P.K. Baumann, R.J. Nemanich, Characterization of copper-diamond (100), (111), and (110) interfaces: Electron affinity and Schottky barrier, Phys. Rev. B 58 (3) (1998) 1643–1654, https://doi.org/10.1103/PhysRevB.58.1643.
[23] P.K. Baumann, R.J. Nemanich, Electron affinity and Schottky barrier height of metal–diamond (100), (111), and (110) interfaces, J. Appl. Phys. 83 (4) (1998) 2072–2082, https://doi.org/10.1063/1.366940.
[24] A.K. Tiwari, J.P. Goss, P.R. Briddon, N.G. Wright, A.B. Horsfall, M.J. Rayson, Electronic and structural properties of diamond (001) surfaces terminated by selected transition metals, Phys. Rev. B Condens. Matter 86 (15) (2012) 155301, https://doi.org/10.1103/PhysRevB.86.155301.
[25] M.C. James, M. Cattelan, N.A. Fox, R.F. Sila, R.M. Silva, P.W. May, Experimental studies of electron affinity and work function from aluminium on oxidised diamond (100) and (111) Surfaces, Phys. Status Solidi B: Basic Solid State Phys. 258 (7) (2021) 2100027, https://doi.org/10.1002/pssb.202100027.
[26] R. Zulkharnay, P.W. May, Experimental evidence for large negative electron affinity from scandium-terminated diamond, J. Mater. Chem. A 11 (2023) 13432–13445, https://doi.org/10.1039/D2TA09199B.
[27] R. Zulkharnay, N.A. Fox, P.W. May, Enhanced electron emission performance and air-surface stability in ScO-terminated diamond for thermionic energy converters, Small 20 (2024) 2405408, https://doi.org/10.1002/smll.202405408].
[28] A. Schenk, A. Tadich, M. Sear, K.M. O'Donnell, L. Ley, A. Stacey, C. Pakes, Formation of a silicon terminated (100) diamond surface, Appl. Phys. Lett. 106 (19) (2015) 191603, https://doi.org/10.1063/1.4921181.

[29] A.K. Schenk, A. Tadich, M.J. Sear, D. Qi, A.T.S. Wee, A. Stacey, C.I. Pakes, The surface electronic structure of silicon terminated (100) diamond, Nanotechnol 27 (27) (2016) 275201, https://doi.org/10.1088/0957-4484/27/27/275201.
[30] A.K. Schenk, M.J. Sear, A. Tadich, A. Stacey, C.I. Pakes, Oxidation of the silicon terminated (100) diamond surface, J. Phys: Cond. Matter 29 (2) (2016) 025003, https://doi.org/10.1088/0953-8984/29/2/025003.
[31] M.J. Sear, A.K. Schenk, A. Tadich, A. Stacey, C.I. Pakes, P-type surface transfer doping of oxidised silicon terminated (100) diamond, Appl. Phys. Lett. 110 (1) (2017) 011605, https://doi.org/10.1063/1.4973602.
[32] J. Beattie, J. Goss, P. Briddon, M. Rayson, Silicon and germanium terminated (001)-(2×1) diamond surface, J. Phys: Cond. Matter 31 (2019), https://doi.org/10.1088/1361-648X/ab2d6c.
[33] M.J. Sear, A.K. Schenk, A. Tadich, B.J. Spencer, C.A. Wright, A. Stacey, C.I. Pakes, Germanium terminated (1 0 0) diamond, J. Phys: Cond. Matter 29 (14) (2017) 145002, https://doi.org/10.1088/1361-648X/aa57c4.
[34] R.F.W. Bader. Atoms In Molecules: a Quantum Theory, Oxford University Press Inc, United States, 1990.
[35] C.J. Fall, N. Binggeli, A. Baldereschi, Deriving accurate work functions from thin-slab calculations, J. Phys: Cond. Matter 11 (13) (1999) 2689–2696, https://doi.org/10.1088/0953-8984/11/13/006.
[36] S. Salustro, G. Sansone, C.M. Zicovich-Wilson, Y. Noël, L. Maschio, R. Dovesi, The A-center defect in diamond: quantum mechanical characterization through the infrared spectrum, Phys. Chem. Chem. Phys. 19 (22) (2017) 14478–14485, https://doi.org/10.1039/C7CP00093F.
[37] R. Dovesi, F. Pascale, B. Civalleri, K. Doll, N.M. Harrison, I. Bush, P. D'Arco, Y. Noël, M. Rérat, P. Carbonnière, M. Causà, S. Salustro, V. Lacivita, B. Kirtman, A. M. Ferrari, F.S. Gentile, J. Baima, M. Ferrero, R. Demichelis, M. De La Pierre, The CRYSTAL code, 1976–2020 and beyond, a long story, J. Chem. Phys. 152 (20) (2020) 204111, https://doi.org/10.1063/5.0004892.
[38] B.P. Pritchard, D. Altarawy, B. Didier, T.D. Gibson, T.L. Windus, New basis set exchange: an open, up-to-date resource for the molecular sciences community, J. Chem. Inform. Model. 59 (11) (2019) 4814–4820, https://doi.org/10.1021/acs.jcim.9b00725.
[39] S. Salustro, F. Pascale, W.C. Mackrodt, C. Ravoux, A. Erba, R. Dovesi, Interstitial nitrogen atoms in diamond. A quantum mechanical investigation of its electronic and vibrational properties, Phys. Chem. Chem. Phys. 20 (24) (2018) 16615–16624, https://doi.org/10.1039/C8CP02484G.
[40] S. Conejeros, M.Z. Othman, A. Croot, J.N. Hart, K.M. O'Donnell, P.W. May, N. L. Allan, Hunting the elusive shallow n-type donor – an *ab initio* study of Li and N co-doped diamond, Carbon 171 (2021) 857–868, https://doi.org/10.1016/j.carbon.2020.09.065.
[41] D. Vilela Oliveira, J. Laun, M.F. Peintinger, T. Bredow, BSSE-correction scheme for consistent gaussian basis sets of double- and triple-zeta valence with polarization quality for solid-state calculations, J. Comp. Chem. 40 (27) (2019) 2364–2376, https://doi.org/10.1002/jcc.26013.
[42] S.C. North, K.R. Jorgensen, J. Pricetolstoy, A.K. Wilson, Population analysis and the effects of Gaussian basis set quality and quantum mechanical approach: main group through heavy element species, Front. Chem. 11 (2023), https://doi.org/10.3389/fchem.2023.1152500.
[43] U. Mölder, P. Burk, I.A. Koppel, Quantum chemical calculations of geometries and gas-phase deprotonation energies of linear polyyne chains, Int. J. Quantum Chem. 82 (2) (2001) 73–85, https://doi.org/10.1002/1097-461X(2001)82:2<73::AID-QUA1025>3.0.CO;2-H.